Defect-rich N/O-co-doped porous carbon frameworks as anodes for superior potassium and sodium-ion batteries

BAI Ling[1], LIU Qian[1], HONG Tao[1], LI Hao-ran[1], ZHU Fang-yuan[2], LIU Hai-gang[2,*], LI Zi-quan[1,*], HUANG Zhen-dong[1,*]

（1. *State Key Laboratory for Organic Electronics and Information Displays & Jiangsu Key Laboratory for Biosensors, Institute of Advanced Materials, Jiangsu National Synergetic Innovation Center for Advanced Materials, Nanjing* 210023, *China*;
2. *Shanghai Advanced Research Institute, Shanghai* 201210, *China*）

Abstract: Carbon with its high electrical conductivity, excellent chemical stability, and structure ability is the most promising anode material for sodium and potassium ion batteries. We developed a defect-rich porous carbon framework (DRPCF) built with N/O-co-doped mesoporous nanosheets and containing many defects using porous g-C_3N_4 (PCN) and dopamine (DA) as raw materials. We prepared samples with PCN/DA mass ratios of 1/1, 2/1 and 3/1 and found that the one with a mass ratio of 2/1 and a carbonization temperature of 700 °C in an Ar atmosphere (DRPCF-2/1-700), had a large specific surface area with an enormous pore volume and a large number of N/O heteroatom active defect sites. Because of this, it had the best pseudocapacitive sodium and potassium ion storage performance. A half battery of Na//DRPCF-2/1-700 maintained a capacity of 328.2 mAh g^{-1} after being cycled at 1 A g^{-1} for 900 cycles, and a half battery of K//DRPC-2/1-700 maintained a capacity of 321.5 mAh g^{-1} after being cycled at 1 A g^{-1} for 1200 cycles. The rate capability and cycling stability achieved by DRPCF-2/1-700 outperforms most reported carbon materials. Finally, ex-situ Raman spectroscopy analysis result confirms that the filling and removing of K^+ and Na^+ from the electrochemically active defects are responsible for the high capacity, superior rate and cycling performance of the DRPCF-2/1-700 sample.

Key words: Defect-rich porous carbon; N/O-co-doping; Anode materials; Sodium ion batteries; Potassium ion batteries

1 Introduction

In the past 30 years, lithium-ion batteries (LIBs) have dominated the primary market of portable power sources due to their high energy density[1–3]. However, the price of LIBs keeps increasing with the expansion of market to large-scale energy storage plants and electric vehicles[3]. Therefore, sodium/potassium-ion batteries (SIBs/PIBs) have attracted significant attention due to their potentially low production prices derived from the abundance of sodium and potassium[4–6]. Unfortunately, the much larger radius of Na^+ and K^+ than that of Li^+ seriously increases the diffusion barrier within the solid lattice, which causes more remarkable volume changes of both anode and cathode materials during the (de)intercalation processes[7–9]. The heavier mass of Na^+/K^+ also results in a relatively lower specific capacity of both anode and cathode materials[10]. Therefore, both SIBs and PIBs demonstrate a lower energy density, poorer rate capability and cyclic stability than LIBs, which seriously limits the development and application of both SIBs and PIBs[11–14].

Hence, scientists have made significant efforts to search for more suitable anode materials with low production cost, high specific capacity, superior rate capability, and excellent cyclic stability. Because the mass-specific capacities of anode materials are much higher than those of cathode materials, anode materials are considered as the critical limitation of the energy density of both SIBs and PIBs[14–17]. As reported, carbonaceous materials exhibit higher electrical conductivity, better chemical stability, and better capabil-

Received date: 2024-07-04; **Revised date:** 2024-09-28
Corresponding author: LIU Hai-gang, Associate Professor. E-mail: liuhg@sari.ac.cn;
LI Zi-quan, Professor. E-mail: lizq@njupt.edu.cn;
HUANG Zhen-dong, Professor. E-mail: iamzdhuang@njupt.edu.cn
Author introduction: BAI Ling, Experimentalist. E-mail: iamlbai@njupt.edu.cn
Supplementary data associated with this article can be found in the online version.

ity to alleviate the enormous volume expansion[18–21] than alloy-based materials[12,22], metal phosphides[23,24], selenides[25,26] and sulfides[27,28]. Therefore, carbonaceous materials become extremely attractive anodes for SIBs and PIBs[15,16,29–32].

Defects, such as topological, vacancy, edge and complex defects, have been considered the most essential active sites for Na^+ and K^+ storage[33–35]. On the contrary, the defect-free graphite structure is unsuitable for accommodating Na^+ and K^+ due to the narrow interlayer space. Therefore, researchers have applied defect engineering as an effective strategy to generate defect-rich carbon nanostructures with enhanced energy storage performance[36,37]. N, O, P, S, and F were reported as the typical heteroatoms to dope carbonaceous materials for generating massive active defect sites[38]. For example, N/O co-doped carbon network[39–41], P/N co-doped 3D porous carbon[42,43] and nanoporous nitrogen-doped carbon[44,45] all exhibit attractive Na/K-ion storage properties. The reported density functional theory (DFT) calculation results also indicated that the co-doping of carbon materials by N and O could significantly increase the absorption energy of carbon materials to K^+ and accelerate the charge migration, in turn enhancing the capacity and rate capability of carbon materials for potassium ion storage[46–49].

Recently, a non-toxic, low-cost and environment-friendly material, graphitic carbon nitride (g-C_3N_4), has been developed as a photocatalyst due to its visible light absorption, tunable bandgap and accessible synthesis methods[50,51]. Herein, we develop a series of 3D defect-rich porous carbon frameworks (DRPCF) built with N/O-co-doped carbon nanosheets using porous g-C_3N_4 as a precursor. As an anode material for both SIBs and PIBs, DRPCFs exhibit high rate capability and long-term cyclic stability with a reversible specific capacity of 328.2 and 321.5 mAh g^{-1} at a current density of 1 A g^{-1} over 900 and 1 200 cycles, respectively. Benefitting from the defect-rich porous structure, the electrochemical performance of the obtained DRPCF outperforms most reported carbonaceous materials.

2 Experimental

2.1 Preparation of porous g-C_3N_4 (PCN)

A direct thermal polymerization method was applied to synthesize the PCN precursor. Typically, 20 g of urea powder was mixed uniformly with 1 g of citric acid in an agate mortar for 10 min. The obtained mixture was placed into a 100 mL crucible. Then, the covered crucible was placed in a muffle furnace. Successively, the furnace was heated at a ramping rate of 2 °C min^{-1} and held at 550 °C for 4 h. Finally, the desired PCN was obtained after cooling in the furnace for the following characterization and applications.

2.2 Preparation of defect-rich porous carbon framework (DRPCF)

Firstly, 3 g of trihydroxymethylaminomethane (Tris) were thoroughly dissolved into 85 mL of deionized water under magnetic stirring at room temperature for 10 min to obtain a Tris alkaline solution with a concentration of 0.29 mol L^{-1}. Subsequently, diluted hydrochloric acid with a concentration of 1.164 mol L^{-1} was prepared by mixing 37% concentrated hydrochloric acid and deionized water in a volume ratio of 9∶1. Then, a Tris HCl buffer solution with a pH value of 8 was obtained by adding 15 mL of as-prepared diluted hydrochloric acid into the as-prepared Tris alkaline solution. Continuously, 200 mg of PCN precursor powder and 100 mg of dopamine were weighed and successfully dissolved into the as-prepared Tris HCl buffer solution. After 30 min of ultrasonication treatment and magnetic stirring at room temperature for 24 h, the obtained black mixed suspension was washed and separated through centrifugation at 13 000 r min^{-1} for 20 min each time. After washing with ethanol for 3 times, the centrifugation products, namely polydopamine-coated PCN (PCN/PDA-2/1), were dried in a blast drying oven at 60 °C for 10 h and collected for further thermal treatment. Here, the controlled PCN/PDA-3/1 and PCN/PDA-1/1 were prepared by the same procedure with the mass ratios of PCN to dopamine at 3∶1 and 1∶1, respectively.

The obtained PCN/PDA powders were put in a

porcelain boat and sealed in a tube furnace. After being carbonized under an argon atmosphere at 550, 700, 850 and 1 000 °C for 4 h with a heating rate of 5 °C min^{-1}, the final DRPCF products were obtained and marked as DRPCF-2/1-550, DRPCF-2/1-700, DRPCF-2/1-850, DRPCF-2/1-1000, DRPCF-3/1-700, and DRPCF-1/1-700, where 550, 700, 850 and 1000 are the ratio-carbonization temperatures.

2.3 Characterization

A Bruker X-ray powder diffractometer (D8 advance A25, Cu-*K*a radiation, λ = 1.541 8 Å), a scanning electron microscope (SEM, HITACHI S4800), and a high-resolution transmission electron microscope (HRTEM, operated at 300 kV, FEI Talos F200X) were used to characterize the crystal structure, morphology and element distribution mapping of as-prepared PCN precursor and DRPCFs. The chemical and morphological structure within the as-prepared DRPCFs were analyzed by Fourier transform infrared (FT-IR) spectroscopy using a Nicolet 380 FT-IR spectrometer from 400 to 4 000 cm^{-1} regimes and Raman spectroscopy (Aramis, HORIBA) with a 532 nm laser. X-ray photoelectron spectroscopy (XPS, KRATOS Axis Supra) calibrated based on the binding energy of the C 1s core peak located at 284.8 eV was used to determine the constituent element compositions and valence states of as-prepared DRPCFs. A Micromeritics ASAP 2020 analyzer was applied to evaluate the pore sizes and specific surface areas of DRPCFs.

2.4 Electrochemical Measurements

Assembly and disassembly of half potassium ion batteries (HPIBs) and half sodium-ion batteries (HSIBs) were done in an ultrapure Ar gas-filled glove box. The electrochemical performances of all DRPCF anodes were evaluated in HPIBs and HSIBs. The applied counter and reference electrodes for HPIBs and HSIBs were K and Na metals, respectively. The working electrodes were the composite electrodes of DRPCFs prepared by coating a homogeneous aqueous slurry of the as-prepared DRPCF powder with Kejten black (ECP600JD, AkzoNobel, 20%), carboxymethylcellulose sodium (CMC, DS=0.7, 200–500 mPa.s, 10%) onto copper foils by using a doctor blade to a thickness of 50 μm. Subsequently, the DRPCF electrodes were vacuum-dried at 65 °C for 12 h. Then, the dried DRPCF electrodes were punched into discs of a diameter 12 mm. The mass loading of the active DRPCFs was ~ 0.6 mg cm^{-2}. 5 mol L^{-1} potassium bis(fluorosulfonyl)amide (KFSI) and 1 mol L^{-1} $NaPF_6$ dissolved in DIGLYME (DoDoChem) were used as the electrolyte for HPIBs and HSIBs, respectively. The separators for HPIBs and HSIBs are glass fibers (GE Whatman, GF/A-1820-125). Galvanostatic (dis)charging tests were carried out on a Land battery testing system (CT2001A, Wuhan Land) within the voltage window of 0.01–3 V (vs. K^+/K) and 0.01 –2.5 V (vs. Na^+/Na). The mass-specific capacity was calculated based on the mass of active materials. Cyclic voltammetry (CV) tests were conducted at 0.01 to 3 V versus K/ K^+ and 0.01 to 2.5 V versus Na/ Na^+ at scanning rates of 0.2, 0.4, 0.6, 0.8 and 1 mV s^{-1}. Electrochemical impedance spectroscopy (EIS) was carried out in the 100 MHz–0.01 Hz at an amplitude of 10 mV. Galvanostatic intermittent titration technique (GITT) was conducted on the assembled HPIBs and HSIBs using DRPCF-2/1-700 as the anode material to investigate the kinetic properties of DRPCF within both HPIBs and HSIBs. DRPCF electrodes discharged/charged to various states were prepared by electrochemically discharging the assembled HPIBs and HSIBs to the voltage of 2.5, 2.0, 1.5, 1.0, 0.5, 0.01 V or successively recharging the assembled HPIBs to 0.5, 1, 1.5, 2.0, 2.5 and 3 V at a current density of 100 mA g^{-1}. The tested HPIBs and HSIBs were disassembled in the glove box and washed with DME to remove the rudimentary electrolyte. Finally, the obtained electrodes were put into the small transition cabin of the glove box and dried by vacuuming the transition cabin. Ex-situ Raman spectroscopy and HR-TEM coupled with EDX were conducted to investigate the potassium/sodium ion storage mechanism of the newly developed DRPCFs.

3 Results and discussion

Fig. S1 presents the XRD patterns and SEM images of PCN precursors prepared following the pro-

cesses illustrated in Fig. 1a. As shown in Fig. S1, a broad and sharp peak centered at 27.0° can be observed from the XRD patterns of PCN. This diffraction peak should be ascribed to the (002) crystal plane of heptazine-type g-C_3N_4, similar to our reported g-C_3N_4 for use as a high-performance visible light photocatalyst[51]. The SEM images in Fig. S2a, S2b and S2c show that the as-prepared PCN is micron-sized porous layered particles formed by restacking large g-C_3N_4 nanosheets. The explicit wrinkle indicates an ultrathin characteristic of g-C_3N_4 nanosheets. The particle size is over 5 μm. As shown in Fig. S1, the introduction of PDA did not change the crystal structure of PCN. A uniform PDA coating can be observed from the clear and smooth surface of PCN (Fig. S2d, 2e and 2f).

Fig. 1b, 1c and 1d present the SEM images of DRPCF-2/1-700. Unlike the ultra-large nature of PCN precursor, the obtained DRPCF2/1-700 becomes a 3D porous carbon framework formed by nano-size carbon sheets. TEM image (Fig. 1e) coupled with the corresponding mapping of elements C (Fig. 1f), O (Fig. 1g), N (Fig. 1h) and Cl (Fig. 1i) further prove the porous characteristic and the uniform N/O/Cl-co-doped nature of DRPCF-2/1-700. The uniform distribution of Cl in Fig. 1i further comfirms the uniform mixing of PDA and PCN. Compared to the SEM images shown in Fig. S3a, S3b and S4, the large-size nanosheets of PCN have already evolved into porous nanosheets. However, the sheet thickness of DRPCF-2/1-550 is much higher than that of DRPCF-2/1-700. With the increase of carbonization temperature from

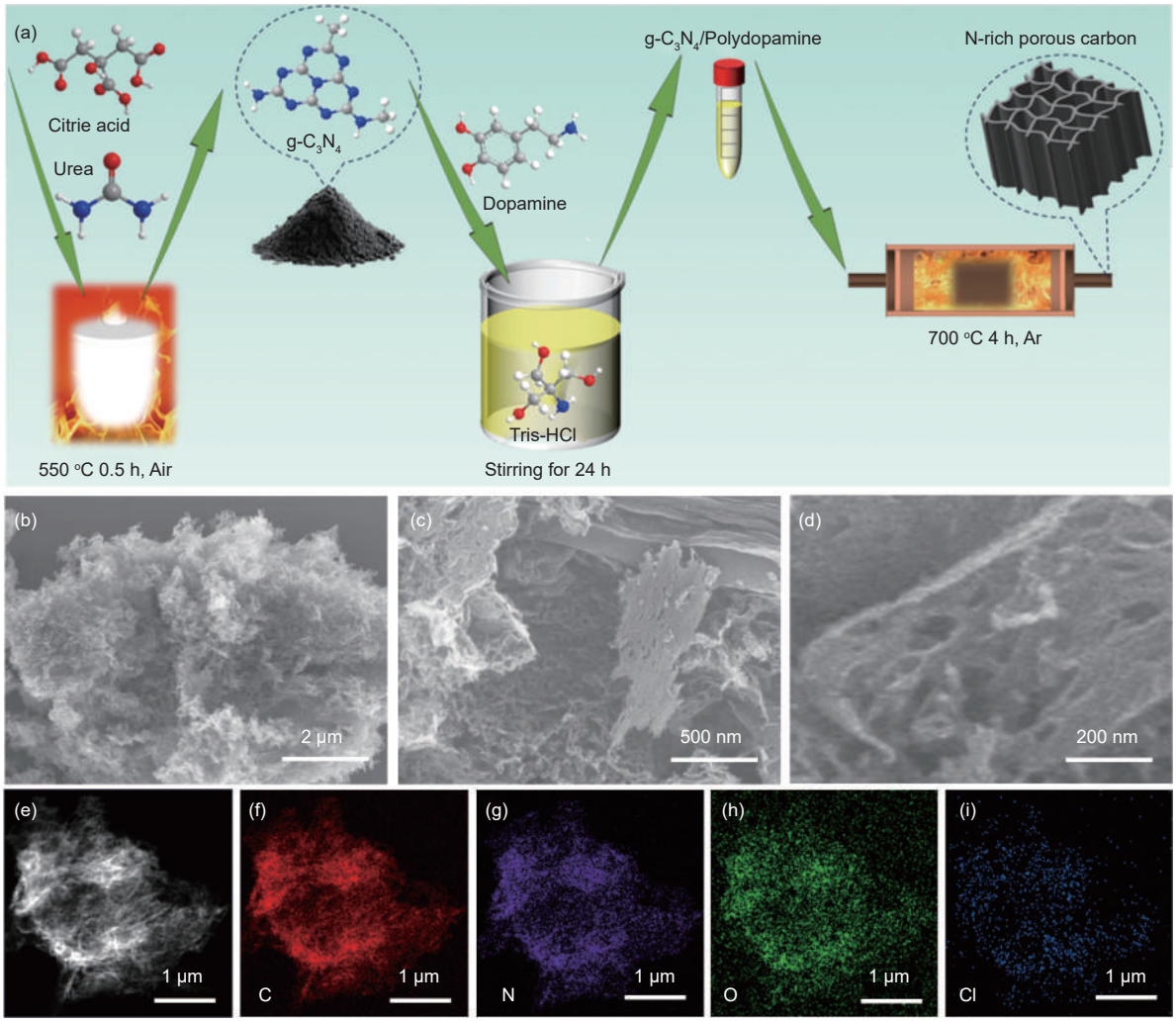

Fig. 1　(a) Schematic illustration for the synthesis process of N/O-co-doped defect-rich porous carbon framework (DRPCF). (b, c, d) SEM images at different magnifications. (e) TEM image and the corresponding element distribution maps of (f) C, (g) N, (h) O and (i) Cl of DRPCF-2/1-700

700 to 850, and 1 000 °C, the thickness of the nanosheet becomes thinner, as present in Fig. S3d, S3e, S3g, S3h and S4. When the carbonization temperature rises from 850 to 1 000 °C, the content of N decreases, as seen in Table S1 and S2. The distribution uniformity gradually decreases, as seen in Fig. S3c, S3f and S3i.

Fig. 2a presents the XRD patterns of DRPCF-2/1 obtained at the carbonization temperature from 550 to 1 000 °C. Compared to the XRD pattern of PCN precursor, the diffraction peaks corresponding to the crystal plane (002) become weaker and broader, which should be caused by the seriously destroyed stacking order along the (002) crystal plane of DRPCF. Moreover, only the diffraction peak of (002) crystal plane belonged to DRPCF-2/1-700 maintains at 27°, the corresponding peaks of DRPCF-2/1-550, DRPCF-2/1-850, DRPCF-2/1-1000, DRPCF-1/1-700 and DRPCF-3/1-700 upshift to 30°, due to the defect-rich structure (Fig. 2a and S5a). This observation indicates that the interlayer space of DRPCF-2/1-700 is the largest.

Fig. 2b provides the Raman spectra of DRPCF-2/1-550, DRPCF-2/1-700, DRPCF-2/1-850 and DRPCF-2/1-1000. The peaks centered at 1 350 cm^{-1} should be generated by the defect-induced vibration of disordered carbons, namely the *D* band. The peaks centered at 1 580 cm^{-1} belong to the *G* band, derived from the sp^2 vibration of graphitization carbons. As summarized in Fig. 2c, the intensity ratio I_D/I_G of the *D* band and *G* band increases from 2.46 for DRPCF-2/1-550 to 2.61 for DRPCF-2/1-700, then decreases to

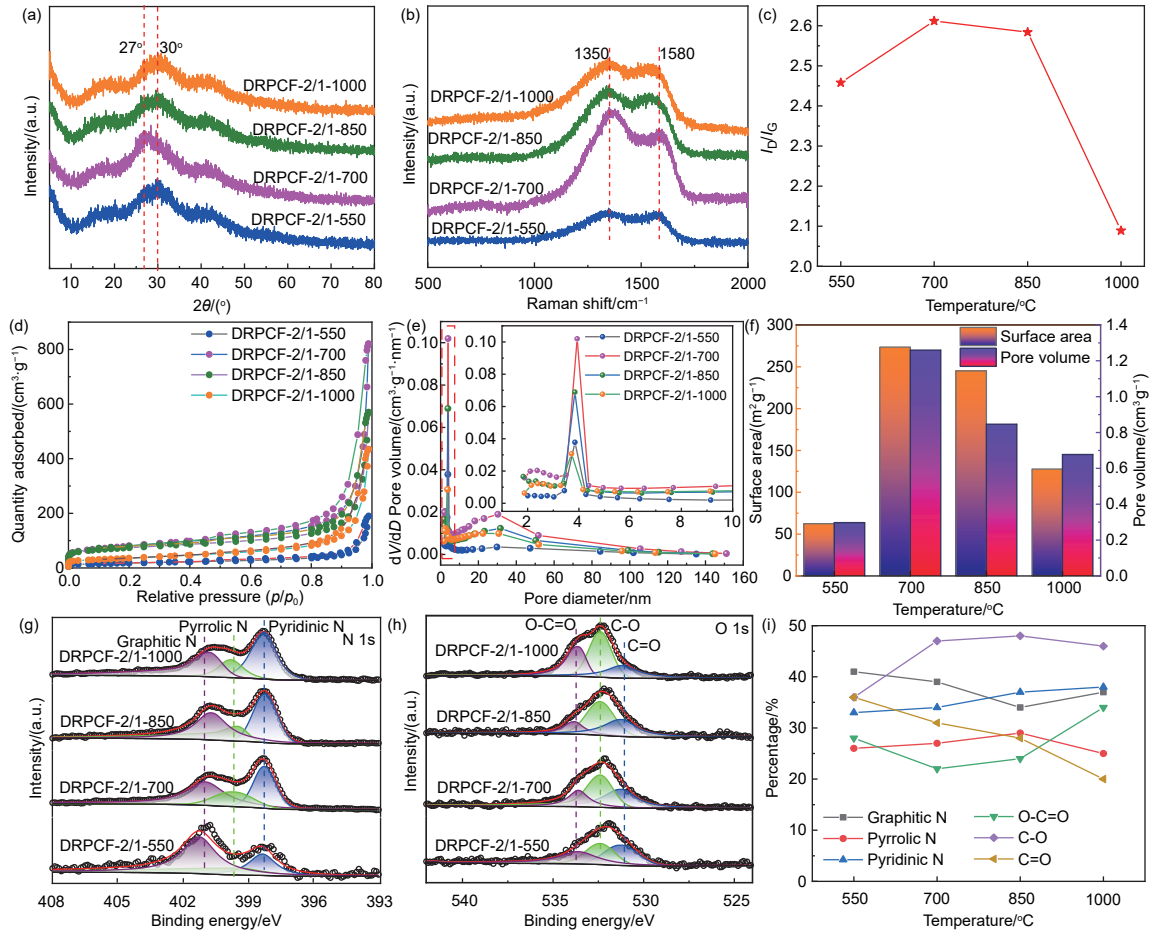

Fig. 2 (a) XRD patterns. (b) Raman spectra. (c) The corresponding I_D/I_G evolution with the carbonization temperature of DRPCF-2/1 obtained at the carbonization temperature from 550 to 1 000 °C. (d) Nitrogen adsorption-desorption isotherms, (e) pore size distributions and (f) the calculated BET specific surface areas and pore volumes of DRPCF-2/1 derived at the carbonization temperatures from 550 to 1 000 °C. (g) The deconvoluted N 1s, (h) O 1s high-resolution X-ray photoelectron spectra (XPS) and (i) the obtained percentages of graphitic, pyrrolic, pyridinic N and carbonyl, carboxyl, hydroxyl O groups of DRPCF-2/1 derived at the carbonization temperature from 550 to 1 000 °C

2.58 for DRPCF-2/1-850, 2.10 of DRPCF-2/1-1000 with increasing the carbonization temperature. The high I_D/I_G values, including 2.48 of DRPCF-3/1-700 and 2.32 of DRPCF-1/1-700 (Fig. S5b), imply all DRPCFs are defect-rich carbon. DRPCF-2/1-700 has the most abundant structural defects, which provides more active sites for K^+/Na^+ storage and results in a large peak shift of DRPCF-2/1-700 in the XRD pattern.

Fig. 2d and 2e show the nitrogen adsorption-desorption isotherms, and the pore size distributions of DRPCF-2/1 with increasing the carbonization temperature from 550 to 1 000 °C. A typical mesoporous structure can be clearly observed from the adsorption-desorption isotherms and the pore size distributions of DRPCF-2/1. The uniform in-plane pore is ~4 nm. The average stacking pore is about 30 nm. Among all DRPCF-1/2, DRPCF-2/1-700 has the largest specific surface area of 273.5 m^2g^{-1} and the largest pore volume of 1.3 cm^3g^{-1} (Fig. 2f).

Fig. S6a presents the full X-ray Photoelectron Spectroscopy (XPS) spectra of DRPCF-2/1-550, DRPCF-2/1-700, DRPCF-2/1-850 and DRPCF-2/1-1000. Only three main elements of C, N and O could be found from the observed full XPS spectra. The corresponding contents of C, N and O in atomic mass ratio is listed in Table S2. This observation is consistent with the element mapping results shown in Table S1. DRPCF-2/1-700 possesses the most abundant N and O heteroatom defects in an atomic fraction of 32.73% and 3.02%, respectively. It is also find that there is a dramatic decrement of N species from DRPCF-2/1-850 to DRPCF-2/1-1000 with increasing the carbonization temperature. The deconvoluted N 1s, O 1s and C 1S spectra of DRPCF-2/1-550, DRPCF-2/1-700, DRPCF-2/1-850, and DRPCF-2/1-1000 are displayed in Fig. 2g, 2h and S6b, respectively. As summarized in Fig. 2i, more than 60% of N species are electrochemically active pyrrolic and Pyridinic N groups.

Galvanostatic charge/discharge measurements at the current densities from 0.1 to 5 A g^{-1} and long-term cyclic measurements at 1 A g^{-1} were conducted to investigate the potassium and sodium ion storage properties. The electrochemical performance in Fig. 3a and 3b demonstrates that all DRPCFs have a good rate capability to store K^+. Especially, DRPCF-2/1-700 shows the best rate performance, namely, 337, 311, 272, 235, 197 and 144 mAh g^{-1} at 100, 200, 500, 1 000, 2 000 and 5 000 mA g^{-1}, respectively. Fig. S7 and 3c are the initial (dis)charge profiles at 0.1 A g^{-1} and the following cycles at 0.2 to 5 A g^{-1}. Fig. S8 and S9 show the corresponding (dis)charging curves at different rates for all other DRPCFs. The slope profiles indicate that surface absorption and pseudocapacitive defects are the main capacity contributors. After being cycled at 1 A g^{-1} for 1 200 times, the specific charge capacity of DRPCF-2/1-700 anode materials stabilize at 323 mAh g^{-1}. Compared to most of the reported counterparts[52–58], the potassium ion storage performance of DRPCF-2/1-700 is much superior (Fig. 3e).

Cyclic voltammetry (CV) measurements were conducted at scan rates from 0.2 to 1 mV s^{-1} to understand the potassium-ion storage mechanism. The obtained CV curves are shown in Fig. 3f. The capacitive contributions to the total capacities of DRPCF-2/1-700 were calculated using the redox peak currents of the CV curves. As shown in Fig. 3g and 3h, the capacitive contribution to the total capacities of DRPCF-2/1-700 are 62.3%, 69.4%, 75.4%, 77.1% and 78.0% at scan rates of 0.2, 0.4, 0.6, 2.0 and 5.0 mV s^{-1}, respectively. This observation further confirms that the surface absorption and hetero-defect derived pseudocapacitance mainly control the electrochemical behavior of DRPCF-2/1-700. Fig. S10 provides the CV curves of all as-prepared DRPCFs in HPIBs obtained at the scanning rate of 0.2 mV s^{-1}, demonstrating a similar redox behavior.

Fig. 4a and 4b present the testing results obtained from ex-situ Raman spectroscopy to reveal the potassium ion storage mechanism of as-developed DRPCF-2/1-700. During the discharge and recharge process of HPIBs at 100 mA g^{-1}, no evident peak shift can be found from the Raman spectra in Fig. 4a and 4b. However, it is interesting to find that the intensity ratio of I_D/I_G almost linearly decreases from 2.98 of

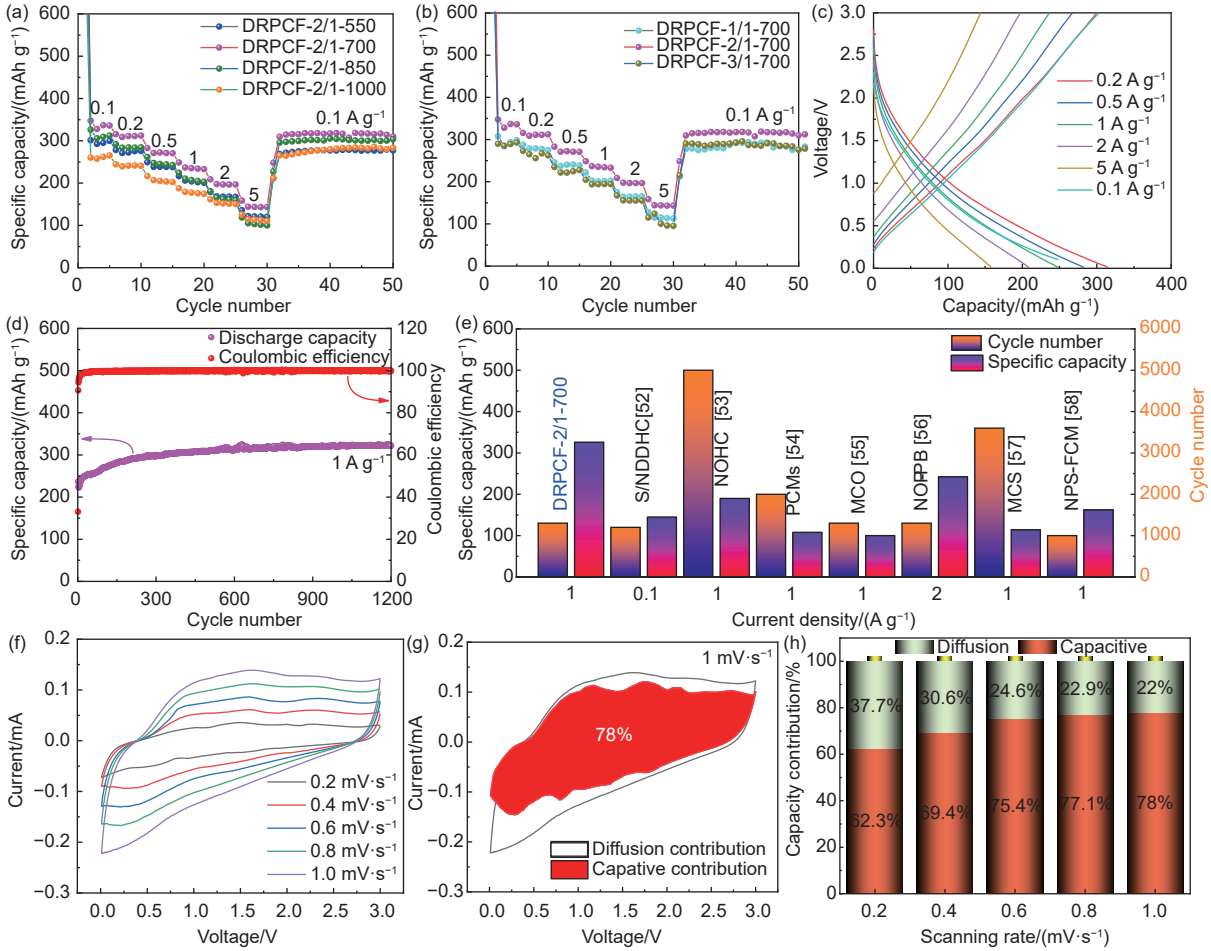

Fig. 3 The potassium ion storage performance of as-prepared DRPCF: (a) Rate performance of half potassium ion batteries (HPIBs) using DRPCF-2/1 obtained at the carbonization temperature from 550 to 1 000 °C as anode materials. (b) Rate performance of HPIBs using DRPCF-1/1-700, DRPCF-2/1-700 and DRPCF-3/1-700 as anode materials. (c) The corresponding galvanostatic charge/discharge profiles at different current densities from 0.1 to 5 A g^{-1}. (d) Long-term cyclic performance at 1 A g^{-1} of HPIBs using DRPCF-2/1-700 as the anode material. (e) The potassium ion storage performance comparison between present work with other reported counterparts[52–58]. (f) The cyclic voltammetry (CV) curves measured at the scanning rates from 0.2 to 1.0 mV s^{-1}. (g) The calculated capacitive contribution of HPIBs using DRPCF-2/1-700 as the anode material at 1.0 mV s^{-1} and (h) the corresponding diffusion and capacitive capacity contribution of HPIBs using DRPCF-2/1-700 as the anode materialevolved with the scanning rates from 0.2 to 1.0 mV s^{-1}

the initial DRPCF-2/1-700 electrode to 2.0 of the electrode discharged to 0.01 V, successively, the intensity ratio of I_D/I_G almost linearly and reversely increase from 2.0 to 2.83 of electrode recharged to 3.0 V (Fig. 4c). The observed results indicate that during the discharge process, the insertion of K^+ can effectively reduce the defects of the DRPCF. The extraction of K^+ during the recharge process can recover most of the defects within the DRPCF.

Fig. 4d displays the galvanostatic intermittent titration technique (GITT) measurement profiles conducted at a constant current of 100 mA g^{-1} for 8 min, followed by 180 min relaxation after each cycle used to evaluate the K^+ diffusion in DRPCF-2/1-700. The calculated K^+ diffusion coefficient (D_K) is in the 10^{-11} $cm^2 \cdot s^{-1}$ range, similar to other reported carbon materials. During the initial discharge process, potassium ions are adsorbed on the material surface and gradually get saturated. The interaction among K^+ results in the gradual decrease of D_K with the increase of surface K^+, as shown in Fig. 4e. Due to the defect-rich porous structure of DRPCF-2/1-700, the active defect sites can accommodate more K^+ during the discharge process. Therefore, the D_K value can remain constant in a long-term discharge period. When all the defects are saturated, the D_K value gradually decreases again. During the charging process, the D_K value decreases with increasing potential and decreasing concentra-

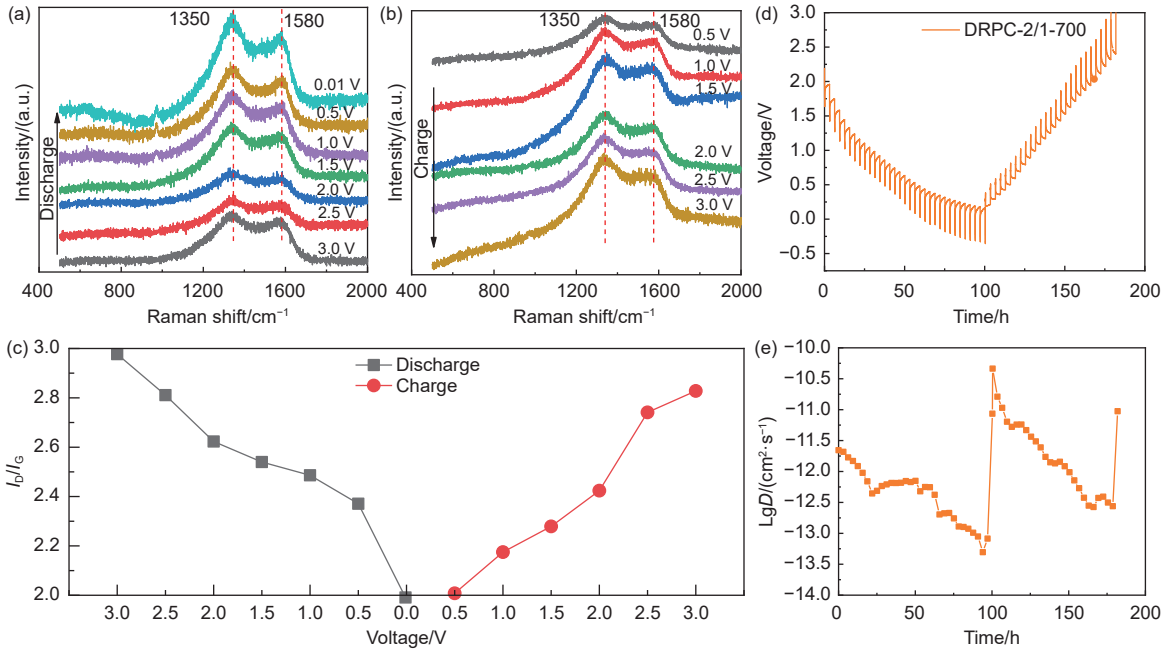

Fig. 4　(a, b) Ex-situ Raman spectra of discharge and recharge DRPCF-2/1-700 electrodes within HPIBs, and (c) the corresponding I_D/I_G evolved with the different discharge/charge states. (d) Galvanostatic intermittent titration technique (GITT) measurement results of K// DRPCF-2/1-700 HPIBs and (e) the calculated diffusion coefficient of K^+ within the DRPCF-2/1-700 electrodes

tion of K^+. This result indicates that the K^+ intercalation/deintercalation process is reversible.

To demonstrate the versatile properties of the as-prepared DRPCFs, all electrochemical measurements done in HPIBs have been done again using DRPCFs as anode materials for HSIBs. The galvanostatic discharge/charge measurement results in Fig. 5a and 5b imply that DRPCF-2/1-700 exhibits the highest specific capacity and the best rate capability for Na^+ storage. The Half sodium-ion batteries (HSIBs) using DRPCF-2/1-700 as the anode material could deliver a specific capacity of 342, 284, 256, 240, 225 and 206 mAh g^{-1} at the current density of 0.1, 0.2, 0.5, 1, 2 and 5 A g^{-1}, respectively. The rate performance and initial coulombic efficiency of DRPCF-2/1-700 as the anode material for HSIBs are higher than those of HPIBs. As shown in Fig. 5c and S11, the initial coulombic efficiency of DRPCF-2/1-700 as the anode material for HSIBs at 0.1 A g^{-1} is 67%. With the gradual activation during the discharge/charge cycles, the HSIBs using DRPCF-2/1-700 as the anode material could retain a specific capacity of 328 mAh g^{-1} after 900 cycles at 1 A g^{-1} with high coulombic efficiency (Fig. 5d). Compared with other reported counterparts[42,59–63] shown in Fig. 5e, the sodium ion storage performance achieved by DRPCF-2/1-700 is superior. A relatively obvious redox peak pair lower than 0.25 V can be found from the CV curves of DRPCF-2/1-700 and other as-prepared DRPCFs (Fig. 5f and S12). A short discharge plateau could also be observed from the typical discharge profile shown in Fig. 5c, S13 and S14. Moreover, the capacitive contributions of Na//DRPCF-2/1-700 HSIBs are 76.1%, 82.4%, 84.4%, 86.2% and 88% at the scanning rates of 0.2, 0.4, 0.6, 0.8 and 1 mV s^{-1}. The specific surface area, pore volume and defect-rich structure should account for the superior K^+/Na^+ storage properties.

The ex-situ Raman spectroscopy results shown in Fig. 6a, 6b and 6c further confirm that the filling and removing of K^+ and Na^+ from the sites of the electrochemically active defects should be responsible for the high capacity, superior rate and cyclic performance of both Na//DRPCF-2/1-700 HSIBs and K//DRPCF-2/1-700 HPIBs. The sodium ion diffusion coefficient (D_{Na}) calculated based on the GITT measurement results of Na//DRPCF-2/1-700 HSIBs is also in the 10^{-11} $cm^2 \cdot s^{-1}$ range, which is slightly higher than D_K in Na//DRPCF-2/1-700 HSIBs.

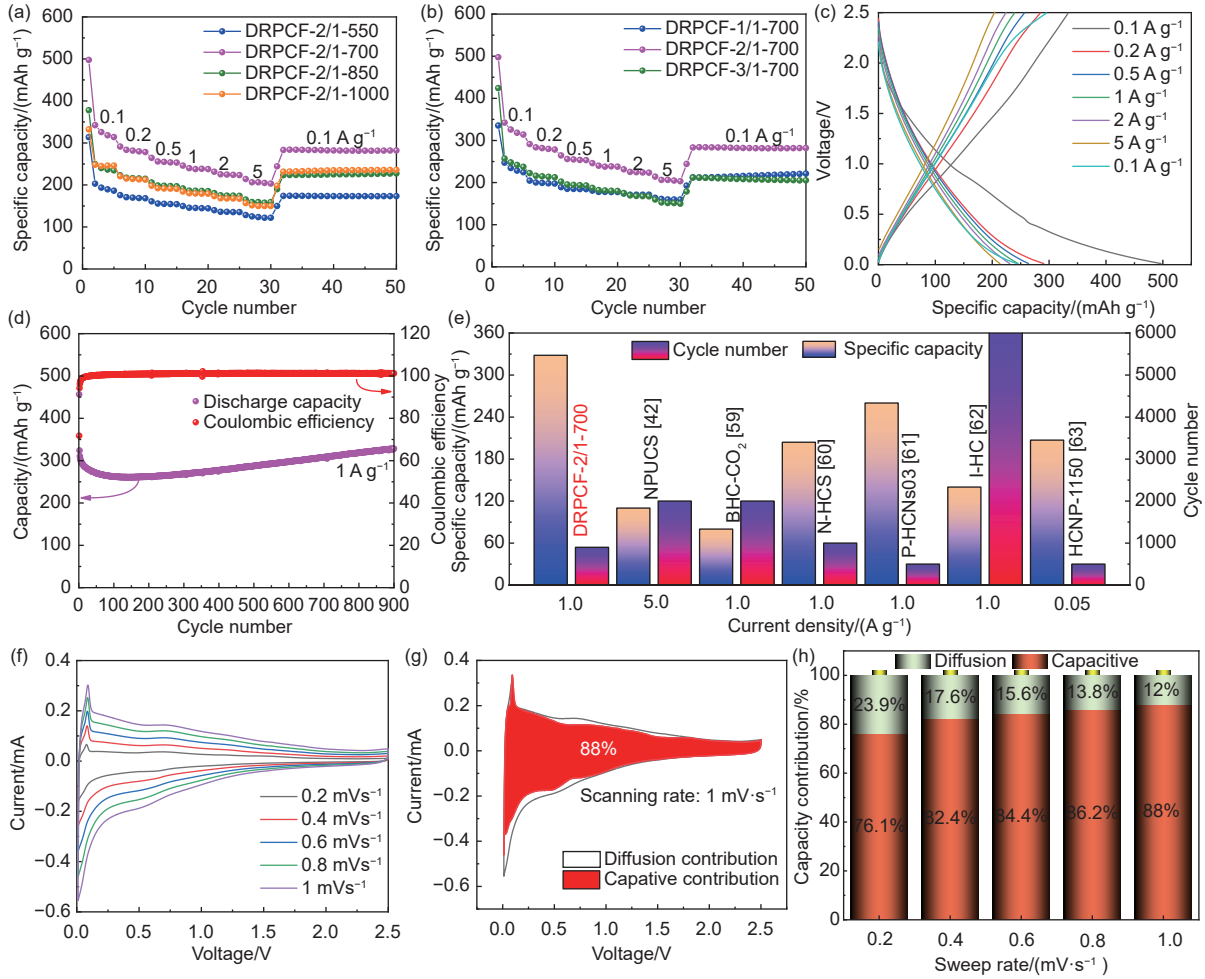

Fig. 5 The sodium ion storage performance of as-prepared DRPCF: (a) Rate performance of half sodium-ion batteries (HSIBs) using DRPCF-2/1 obtained at the carbonization temperature from 550 to 1 000 °C as anode materials. (b) Rate performance of HSIBs using DRPCF-1/1-700, DRPCF-2/1-700 and DRPCF-3/1-700 as anode materials. (c) The corresponding galvanostatic charge/discharge profiles at different current density from 0.1 to 5 A g^{-1}, (d) long-term cycle performance at 1 A g^{-1} of HSIBs using DRPCF-2/1-700 as anode materials, and (e) the comparison of sodium ion storage performance between present work with other reported counterparts[42,59–63]. (f) The cyclic voltammetry (CV) curves measured at the scanning rates from 0.2 to 1.0 mV s^{-1}. (g) The calculated capacitive contribution of HSIBs using DRPCF-2/1-700 as the anode material at 1.0 mV s^{-1} and (h) the corresponding diffusion and capacitive capacity contribution of Na//DRPCF-2/1-700 HSIBs evolved with the scanning rates from 0.2 to 1.0 mV s^{-1}

Fig. S15 displays the electrochemical impedance spectra (EIS) of potassium ion and sodium ion half batteries assembled with the electrodes made of as-prepared different DRPCFs. The results further confirm that the as-prepared DRPCF-2/1-700 is the desirable anode material because of the relatively smaller resistance than other DRPCF materials both in the potassium ion and sodium ion half batteries.

Fig. S16 presents the potassium ion storage performance and the sodium ion storage performance of the half batteries assembled with the electrodes made of 100% Ketjen black, DRPCF-2/1 with 20% Ketjen black and 100% DRPCF-2/1-700. The results indicate that the applied conductive additive, namely Ketjen black, exhibits a certain capability to store both sodium and potassium ion with a lower specific capacity. As shown in Fig. S16, the achieved capacity of half potassium and sodium ion batteries assembled with the electrodes made of 100% Ketjen black can only deliver ~ 100 mAh g^{-1} at 1 A g^{-1}, which is lower than the capacity achieved by half potassium and sodium ion batteries assembled with the electrodes DRPCF-2/1-700 with 20% Ketjen black and 100% DRPCF-2/1-700, especially in half sodium ion batteries. Therefore, Ketjen black can help to obviously improve the rate capability of DRPCF-2/1-700, but its contribution to capacity of DRPCF-2/1-700 is low.

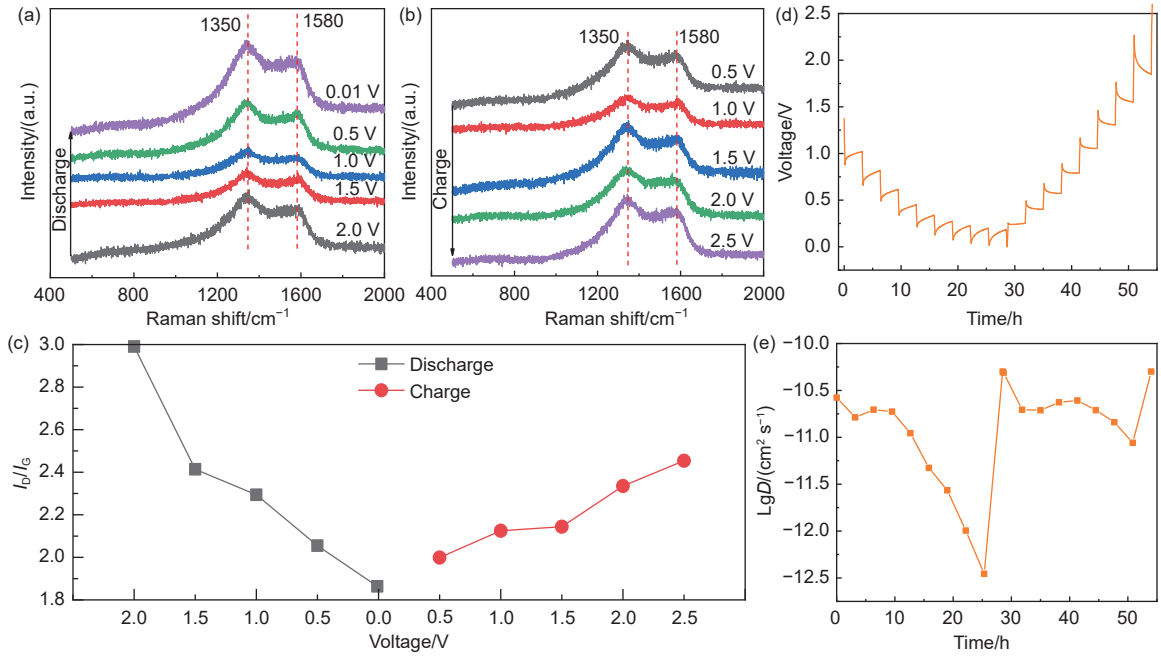

Fig. 6　(a, b) Ex-situ Raman spectra of discharged and re-changed DRPCF-2/1-700 electrodes within HSIBs, and (c) the corresponding I_D/I_G evolved with the different discharge/charge states. (d) Galvanostatic intermittent titration technique (GITT) measurement results of Na//DRPCF-2/1-700 HSIBs and (e) the calculated diffusion coefficient of Na^+ within the DRPCF-2/1-700 electrode during the discharge and charge processes

4　Conclusions

This work developed a defect-rich porous carbon framework (DRPCF) built with N/O-co-doped mesoporous nanosheets using porous g-C_3N_4 and dopamine as precursors. The carbonization temperature and mass ratio of porous g-C_3N_4 and dopamine are modified to optimize the morphology, composition and structure. The measurement results of SEM, TEM element mapping, XPS, BET, and Raman spectroscopy imply that DRPCF-2/1-700, prepared by using porous g-C_3N_4 and dopamine in a mass ratio of 2∶1 as precursors followed by carbonization at 700 °C, has the largest specific surface area with the largest pore volume, possesses highest N/O heteroatom active defect sites. Taking advantage of defect-rich characteristics and a large specific surface area with a large pore volume, the newly developed DRPCF-2/1-700 demonstrates superior pseudocapacitive behavior dominated sodium and potassium ion storage performance. As an anode material for both SIBs and PIBs, DRPCF-2/1-700 exhibits high rate and long-term cyclic stability with a reversible specific capacity of 328.2 and 321.5 mAh g^{-1} at a current density of 1 A g^{-1} over 900 and 1 200 cycles, respectively. The electrochemical performance of the obtained DRPCF outperforms most reported carbonaceous materials. The ex-situ Raman spectroscopy results further confirm that the reversible filling and removing K^+ and Na^+ from the electrochemically active defect sites should be responsible for the high capacity, superior rate and cyclic performance of DRPCF-2/1-700.

Acknowledgements

This work was conducted under the auspices of Jiangsu Province Carbon Peak and Neutrality Innovation Program (Industry tackling on prospect and key technology) (BE2022002-4), the National Natural Science Foundation of China (52277219, 61974072), Fund of NJUPT (NY221089, NY220195, NY219110).

References

[1] Cai Y Q, Liu H G, Li H R, et al. Strong coordination interaction in amorphous Sn-Ti-ethylene glycol compound for stable Li-ion storage[J]. Energy Materials and Devices, 2023, 1: 9370013.

[2] Li M, Lu J, Chen Z, et al. 30 years of lithium-ion batteries[J]. Advanced Materials, 2018, 30: 1800561.

[3] Z, Zhang B. Weakly solvating electrolytes for next-generation lithium batteries: Design principles and recent advances[J]. Energy

Materials and Devices, 2023, 1: 9370003.

[4] Min X, Xiao J, Fang M, et al. Potassium-ion batteries: Outlook on present and future technologies[J]. Energy & Environmental Science, 2021, 14: 2186-2243.

[5] Wang M Y, Li Y, Yao S S, et al. Conversion mechanism of $NiCo_2Se_4$ nanotube sphere anodes for potassium-ion batteries[J]. Energy Materials and Devices, 2023, 1: 9370001.

[6] Chen M, Liu Q, Hu Z, et al. Designing advanced vanadium-based materials to achieve electrochemically active multielectron reactions in sodium/potassium-ion batteries[J]. Advanced Energy Materials, 2020, 10: 2002244.

[7] Xu Y S, Guo S J, Tao X S, et al. High-performance cathode materials for potassium-ion batteries: Structural design and electrochemical properties[J]. Advanced Materials, 2021, 33: 2100409.

[8] Li Y, Lu Y, Adelhelm P, et al. Intercalation chemistry of graphite: Alkali metal ions and beyond[J]. Chemical Society Reviews, 2019, 48: 4655-4687.

[9] Zhang Z, Wang R, Zeng J, et al. Size effects in sodium ion batteries[J]. Advanced Functional Materials, 2021, 31: 2106047.

[10] Sun Z, Liang H, Wang H, et al. Spatially confined “edge-to-edge” strategy for achieving compact Na^+/K^+ storage: Constructing hetero-Ni/Ni_3S_2 in densified carbons[J]. Advanced Functional Materials, 2022, 32: 2203291.

[11] Pan Q, Tong Z, Su Y, et al. Energy storage mechanism, challenge and design strategies of metal sulfides for rechargeable sodium/potassium-ion batteries[J]. Advanced Functional Materials, 2021, 31: 2103912.

[12] Li Z Q, Wen J Q, Cai Y Q, et al. Hydrated Bi-Ti-bimetal ethylene glycol: a new high-capacity and stable anode material for potassium-ion batteries[J]. Advanced Functional Materials, 2023, 33(22): 2300582.

[13] Chen C, Yang Y, Tang X, et al. Graphene-encapsulated FeS_2 in carbon fibers as high reversible anodes for Na^+/K^+ batteries in a wide temperature range[J]. Small, 2019, 15: 1804740.

[14] Wu X, Chen Y, Xing Z, et al. Advanced carbon-based anodes for potassium-ion batteries[J]. Advanced Energy Materials, 2019, 9: 1900343.

[15] Zhang L, Wang W, Lu S, et al. Carbon anode materials: A detailed comparison between Na-ion and K-ion batteries[J]. Advanced Energy Materials, 2021, 11: 2003640.

[16] Mohan I, Raj A, Shubham K, et al. Potential of potassium and sodium-ion batteries as the future of energy storage: Recent progress in anodic materials[J]. Journal of Energy Storage, 2022, 55: 105625.

[17] Zhao L F, Hu Z, Lai W H, et al. Hard carbon anodes: Fundamental understanding and commercial perspectives for Na-ion batteries beyond Li-ion and K-ion counterparts[J]. Advanced Energy Materials, 2021, 11: 2002704.

[18] Hou H, Qiu X, Wei W, et al. Carbon anode materials for advanced sodium-ion batteries[J]. Advanced Energy Materials, 2017, 7: 1602898.

[19] Tang Z, Zhou S, Huang Y, et al. Improving the initial coulombic efficiency of carbonaceous materials for Li/Na-Ion batteries: Origins, solutions, and perspectives[J]. Electrochemical Energy Reviews, 2023, 6: 8.

[20] Wang D, Zhao H, Zhang C, et al. Low-cost and high-rate porous carbon anode material for potassium-ion batteries[J]. Solid State Ionics, 2022, 381: 115944.

[21] Hong Z, Maleki H, Ludwig T, et al. New insights into carbon-based and MXene anodes for Na and K-ion storage: A review[J]. Journal of Energy Chemistry, 2021, 62: 660-691.

[22] Wu J J, Yuan B, Gu Y Y, et al. Multifunctional layered bismuth oxychloride/ amorphous antimony oxide hetero-hybrids as superior photocatalyst and potassium ion storage materials[J]. Applied Catalysis B-environmental, 2022, 321: 122032-122032.

[23] Li Z, Zheng Y, Liu Q, et al. Recent advances in nanostructured metal phosphides as promising anode materials for rechargeable batteries[J]. Journal of Materials Chemistry A, 2020, 8: 19113-19132.

[24] Yue L, Liang J, Wu Z, et al. Progress and perspective of metal phosphide/carbon heterostructure anodes for rechargeable ion batteries[J]. Journal of Materials Chemistry A, 2021, 9: 11879-11907.

[25] Gong Y, Li Y, Li Y, et al. Metal selenides anode materials for sodium ion batteries: Synthesis, modification, and application[J]. Small, 2023, 19: 2206194.

[26] Hussain I, Sahoo S, Lamiel C, et al. Research progress and future aspects: Metal selenides as effective electrodes[J]. Energy Storage Materials, 2022, 47: 13-43.

[27] Liu Y, Yang C, Zhang Q, et al. Recent progress in the design of metal sulfides as anode materials for sodium ion batteries[J]. Energy Storage Materials, 2019, 22: 66-95.

[28] Lim Y V, Li X L, Yang H Y. Recent tactics and advances in the application of metal sulfides as high-performance anode materials for rechargeable sodium-ion batteries[J]. Advanced Functional Materials, 2021, 31: 2006761.

[29] Liu M, Wang Y, Wu F, et al. Advances in carbon materials for sodium and potassium storage[J]. Advanced Functional Materials, 2022, 32: 2203117.

[30] Wang X, Wang H. Designing carbon anodes for advanced potassium-ion batteries: Materials, modifications, and mechanisms[J]. Advanced Powder Materials, 2022, 1: 100057.

[31] Pothaya S, Poochai C, Tammanoon N, et al. Bamboo-derived hard carbon/carbon nanotube composites as anode material for long-life sodium-ion batteries with high charge/discharge capacities[J]. Rare Metals, 2024, 43: 124-137.

[32] Wang F, Jiang Z, Zhang Y, et al. Revitalizing sodium-ion batteries via controllable microstructures and advanced electrolytes for hard carbon[J]. eScience, 2024, 4: 100181.

[33] Sun Y, Wang H, Wei W, et al. Sulfur-rich graphene nanoboxes with ultra-high potassiation capacity at fast charge: Storage mechanisms and device performance[J]. ACS Nano, 2021, 15: 1652-1665.

[34] Zhang W, Wang H, Liao R, et al. Salt-assisted in-situ formation of N-doped porous carbons for boosting K^+ storage capacity and cycling stability[J]. New Carbon Materials, 2021, 36: 167-178.

[35] Liu X, Ji T, Guo H, et al. Effects of crystallinity and defects of layered carbon materials on potassium storage: A review and prediction[J]. Electrochemical Energy Reviews, 2022, 5: 1-33.

[36] Chen Y, Xi B, Huang M, et al. Defect-selectivity and "order-in-disorder" engineering in carbon for durable and fast potassium storage[J]. Advanced Materials, 2022, 34: 2108621.

[37] Zhang Y, Tao L, Xie C, et al. Defect engineering on electrode materials for rechargeable batteries[J]. Advanced Materials, 2020, 32: 1905923.

[38] Tian Y, Liu N, Li J, et al. Covalent organic frameworks derived F/N co-doped porous carbon for potassium-ion batteries[J]. Journal of Alloys and Compounds, 2023, 952: 169998.

[39] Chong S, Yuan L, Li T, et al. Nitrogen and oxygen co-doped porous hard carbon nanospheres with core-shell architecture as anode materials for superior potassium-ion storage[J]. Small, 2022, 18: 2104296.

[40] Song Z, Di M, Chen S, et al. Three-dimensional N/O co-doped hard carbon anode enabled superior stabilities for sodium-ion batteries[J]. Chemical Engineering Journal, 2023, 470: 144237.

[41] Yang M, Kong Q, Feng W, et al. N/O double-doped biomass hard carbon material realizes fast and stable potassium ion storage[J]. Carbon, 2021, 176: 71-82.

[42] Wu S, Peng H, Xu J, et al. Nitrogen/phosphorus codoped ultramicropores hard carbon spheres for rapid sodium storage[J]. Carbon, 2024, 218: 118756.

[43] Yang W, Zhou J, Wang S, et al. A three-dimensional carbon framework constructed by N/S codoped graphene nanosheets with expanded interlayer spacing facilitates potassium ion storage[J]. ACS Energy Letters, 2020, 5: 1653-1661.

[44] Mehmood A, Ali G, Koyutuerk B, et al. Nanoporous nitrogen doped carbons with enhanced capacity for sodium ion battery anodes[J]. Energy Storage Materials, 2020, 28: 101-111.

[45] Matsagar B M, Yang R X, Dutta S, et al. Recent progress in the development of biomass-derived nitrogen-doped porous carbon[J]. Journal of Materials Chemistry A, 2021, 9: 3703-3728.

[46] Zeng S F, Chen X J, Xu R, et al. Boosting the potassium storage performance of carbon anode via integration of adsorption-intercalation hybrid mechanisms[J]. Nano Energy, 2020, 73: 104807.

[47] Sun Y H, Zhu D M, Liang Z F, et al. Facile renewable synthesis of nitrogen/oxygen co-doped graphene-like carbon nanocages as general lithium-ion and potassium-ion batteries anode[J]. Carbon, 2020, 167: 685-695.

[48] Li S W, Zhu H L, Liu Y, et al. Codoped porous carbon nanofibres as a potassium metal host for nonaqueous K-ion batteries[J]. Nature Communications, 2022, 13: 4911.

[49] Sun Y W, Xiao H, Li H B, et al. Nitrogen/oxygen co-doped hierarchically porous carbon for high-performance potassium storage[J]. Chemistry-A European Journal, 2019, 25: 7359-7365.

[50] Zhang X, Jiang S P. Layered g-C_3N_4/TiO_2 nanocomposites for efficient photocatalytic water splitting and CO_2 reduction: A review[J]. Materials Today Energy, 2022, 23: 100904.

[51] Chang J, Zhang T, Qiu S C, et al. Oxygenated triazine-heptazine heterostructure creates an enormous ascension to the visible light photocatalytic hydrogen evolution performance of porous C_3N_4 nanosheets[J]. Small, 2023, 19: 2301579.

[52] Liu Y, Dai H, Wu L, et al. A large scalable and low-cost sulfur/nitrogen dual-doped hard carbon as the negative electrode material for high-performance potassium-ion batteries[J]. Advanced Energy Materials, 2019, 9: 1901379.

[53] Cui R C, Xu B, Dong H J, et al. N/O dual-doped environment-friendly hard carbon as advanced anode for potassium-ion batteries[J]. Advanced Science, 2020, 7: 1902547.

[54] Chen M, Wang W, Liang X, et al. Sulfur/oxygen codoped porous hard carbon microspheres for high-performance potassium-ion batteries[J]. Advanced Energy Materials, 2018, 8: 1800171.

[55] Xia G, Wang C, Jiang P, et al. Nitrogen/oxygen co-doped mesoporous carbon octahedrons for high-performance potassium-ion batteries[J]. Journal of Materials Chemistry A, 2019, 7: 12317-12324.

[56] Yang M M, Kong Q Q, Feng W, et al. Hierarchical porous nitrogen, oxygen, and phosphorus ternary doped hollow biomass carbon spheres for high-speed and long-life potassium storage[J]. Carbon Energy, 2022, 4: 45-59.

[57] Zheng J, Wu Y, Tong Y, et al. High capacity and fast kinetics of potassium-ion batteries boosted by nitrogen-doped mesoporous carbon spheres[J]. Nano-Micro Letters, 2021, 13: 174.

[58] Zhang X, Huang R, Wu F, et al. Mixed-biomass engineering achieves multi-doped highly-disordered hierarchical flower-like hard carbon for advanced potassium-ion battery[J]. Nano Energy, 2023, 117: 108913.

[59] Wang H, Sun F, Qu Z, et al. Oxygen functional group modification of cellulose-derived hard carbon for enhanced sodium ion storage[J]. ACS Sustainable Chemistry & Engineering, 2019, 7: 18554-18565.

[60] Gaddam R R, Niaei A H F, Hankel M, et al. Capacitance-enhanced sodium-ion storage in nitrogen-rich hard Carbon[J]. Journal of Materials Chemistry A, 2017, 5: 22186-22192.

[61] Wang X, Hou M, Shi Z, et al. Regulate phosphorus configuration in high P-doped hard carbon as a superanode for sodium storage[J]. ACS Applied Materials & Interfaces, 2021, 13: 12059-12068.

[62] Chen J, Hu T, Zou Z, et al. Pre-doping iodine to restrain formation of low-active graphitic-N in hard carbon for significantly boosting sodium storage performance[J]. Carbon, 2022, 186: 193-204.

[63] Xiao L, Cao Y, Henderson W A, et al. Hard carbon nanoparticles as high-capacity, high-stability anodic materials for Na-ion batteries[J]. Nano Energy, 2016, 19: 279-288.